A Numerical Investigation of the Flow Past a Generic Side Mirror and its Impact on Sound Generation

Jonas Ask
Environment and Fluid Dynamics Centre,
Volvo Car Corporation,
SE-405 31 Göteborg, Sweden

Lars Davidson
Professor
Department of Applied Mechanics,
Division of Fluid Dynamics,
Chalmers University of Technology,
SE-412 96 Göteborg, Sweden

The case investigated is the flow past a generic side mirror mounted on a flat plate at the Reynolds number of $Re_D = 5.2 \times 10^5$ based on the mirror diameter. The present work studies both flow and acoustic sources by evaluating two second-order advection schemes, different levels of turbulence modeling, and three different grids. The advection schemes discussed in the present study are a second-order upwind scheme and a monotonic central scheme. The turbulence models investigated cover three levels of modeling. These are the original formulation of the detached eddy simulation (DES) model, the Smagorinsky–Lilly sub-grid scale (SGS) model with near-wall damping, and a dynamic Smagorinsky model. The different grids are as follows: a primary grid where all parameter studies are conducted and a second grid with significantly higher wake resolution and to some extent also increased plate resolution, while maintaining the resolution at the front side of the mirror. The final grid uses a significantly higher plate resolution and a wake resolution similar to that of grid two, but a comparably lower mirror front side resolution as compared with the two other grids. The general outcome of this work is that the estimation of the grid cutoff frequency through a relation of the velocity fluctuation and the grid size matches both the experimental results and trend lines perfectly. Findings from the flow field show that the horseshoe vortex in front of the mirror causes pressure fluctuations with a magnitude exceeding the maximum levels at the rear side of the mirror. Its location and unsteady properties are perfectly captured in the final simulation as compared with the experiments conducted by Daimler–Chrysler. A laminar separation at the front side of the mirror is more or less found for all wall resolved cases except the DES simulation. The third grid fails to predict this flow feature, but it is shown that this effect has no significant effect on either the static pressure sensors at the mirror surface or at the dynamic sensors located downstream of the mirror. The simulation also supports the fundamental frequency based on the eddy convection in the mirror shear layer, which is shown to be twice as high as the frequency peak found in the lateral force spectra.
[DOI: 10.1115/1.3129122]

1 Introduction

Flow induced noise experienced by the driver or passengers of a ground vehicle can be a consequence of different flow or fluid-structure phenomena occurring in low Mach number flows. Exposed components such as side mirrors, A-pillars, rails, tires, and underfloor details generate flow structures, and these are the primary sources of noise generation around the vehicle above approximately 120 km/h. The present work studies the flow past a generic side mirror mounted on a flat plate. This geometry has been the subject of several studies [1–5]. Höld et al. [1] and Siegert et al. [2] conducted both experimental and numerical investigations to predict sound generation and propagation at the Reynolds number of $Re_D = 7.066 \times 10^5$ based on the mirror diameter. They conducted unsteady Reynolds averaged Navier–Stokes (URANS) simulations for three different mesh densities and used an acoustic analogy to compute the radiated sound based on the wall pressure fluctuations and their temporal derivative [6,7]. The simulation in their work covered 0.1 s. A similar study at the Reynolds number of $Re_D = 5.2 \times 10^5$ was reported in Ref. [3], which focused on differences in sound generation and propagation in comparison of URANS and the detached eddy simulation (DES) modeling technique [8]. Their longest simulation covered 0.26 s, and the grid density was twice the highest resolved case in Refs. [1,2]. The results of Rung's DES simulations [3] generally showed an overprediction of the low frequency fluctuating pressure levels for most surface-mounted sensors and microphones. Their findings showed however a major improvement in acoustic results using the DES model as compared with the URANS results.

The generic side mirror is geometrically similar to both the sphere and the cylinder, perhaps best known for their drag crisis around a critical Reynolds number. This great difference in drag force is the consequence of laminar versus turbulent separation over the object. The Reynolds number for the present simulation is close to the critical Reynolds number for both the sphere and the cylinder. According to Schlichting [9], the drag force coefficient over a circular cylinder drops 0.7 over the interval $3.0 \times 10^5 < Re_D < 5.0 \times 10^5$. Similar results are also found for the sphere, where the force coefficient drops 0.31 over the interval $2.5 \times 10^5 < Re_D < 4 \times 10^5$. Constantinescu and Squires [10] mentioned a critical Reynolds number of $Re_{cr} \approx 3.7 \times 10^5$ for the sphere, which agrees well with Schlichting [9]. If an analogy is made between the flow state over the side mirror and the corresponding sphere and cylinder, the boundary layer over the generic side mirror in the present state is close to its critical value. Personal communication and results obtained from Daimler–Chrysler

Contributed by the Fluids Engineering Division of ASME for publication in the JOURNAL OF FLUIDS ENGINEERING. Manuscript received October 19, 2007; final manuscript received March 19, 2009; published online May 14, 2009. Assoc. Editor: Dimitris Drikakis. Paper presented at the 12th AIAA/CEAS Aeroacoustics Conference, Cambridge, MA, May 8–10 2006.

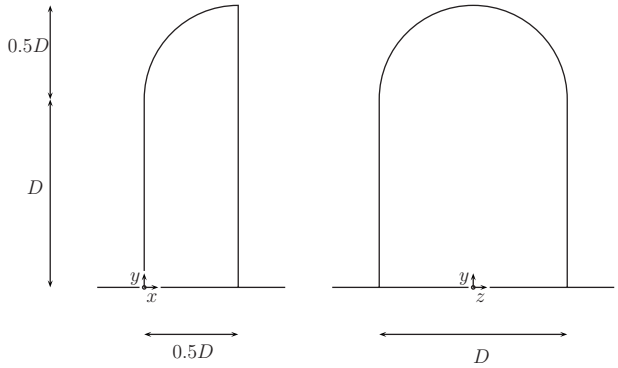

Fig. 1 Mirror geometry: side view and front view, respectively

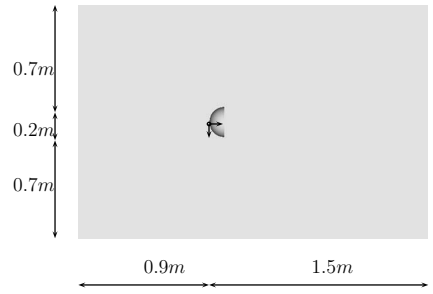

Fig. 2 Mirror and plate: *x–z* plane

[11] showed that the flow state over the mirror is actually subcritical. Regardless of the importance of this flow feature with respect to the sound sources, this constitutes a true challenge for any code and turbulence model to accurately predict both the size and location of the separation point.

With regards to the spatial discretization of the convective fluxes for DES, a general recommendation was made by Strelets [12] and was further applied in Refs. [10,13–15]. He suggested central difference schemes in the wake combined with high-order upwind-biased schemes in the Reynolds averaged Navier–Stokes (RANS) and Euler regions if the pure central differenced scheme proved unstable. The central schemes are known to have stability issues when operating in RANS mode, especially for cells with large aspect ratios. On the other hand, upwind-biased schemes are commonly considered too dissipative for large eddy simulations (LES). Different spatial discretization practices have been reported in the literature in connection with DES. In the most extreme cases, a fifth-order upwind-biased scheme was applied in the Euler and RANS regions combined with a fourth-order central scheme in the wake [14,15]. In Refs. [10,13], a fifth-order upwind scheme was used close to the walls and over the Euler region and was combined with a second-order central difference scheme in the wake region. However, several authors have also reported acceptable results for second and third-order upwind-biased schemes [3,16] involving separated flows.

Although the geometry is fairly simple it poses several challenges. A few are laminar to turbulent transition of the plate boundary layer, a laminar separation close to the mirror trailing edge, prediction of the size and unsteadiness of the horseshoe vortex, and the size of the recirculation zone in the turbulent wake. The main scope of the present paper is therefore to investigate the degree to which these flow features can be predicted using a commercial code, second-order advection schemes, and a mesh topology typically used in industrial applications.

The paper is organized as follows. Section 2 describes the geometry. Section 3 presents the cases considered and discusses the numerical approaches used in the present simulations. The findings from the parameter study are covered in Secs. 4–6, which treat the effects of the two advection schemes, the different turbulence models, and the three grids. This is followed by the results sections, consisting of flow field results (Sec. 7) and fluctuating surface pressure results (Sec. 8) for the most finely resolved cases. Conclusions are given in Sec. 9 and acknowledgments in Sec. 10. An appendix is also included that gives the locations of the static and dynamic pressure sensors (Appendix).

2 Case Description

The mirror consists of a half cylinder with a diameter of $D=0.2$ m blunted by a quarter sphere on top, which gives a total height of $H=0.3$ m. The geometry and origin of the coordinate system are shown in Fig. 1 and its position on the plate is represented in Fig. 2. The upstream part of the mirror will, in the following text, be referred to as the *front side* and the downstream flat side will be referred to as the *rear side*. The Reynolds number based on the mirror diameter is $\mathrm{Re}_D=5.2\times10^5$ with a freestream velocity of 39 m/s.

3 Methodology

The code used in this paper is the unstructured FLUENT commercial solver [17]. It is based on a control volume formulation to convert the governing equations to a solvable set of algebraic equations. The code at the present state uses a collocated scheme with cell-centered storage of both scalars and vectors. In the present work, the incompressible segregated solver is used with an implicit SIMPLEC pressure-velocity coupling algorithm. The domain is bounded by an inlet 3.0 m upstream of the mirror and an outlet 6.0 m downstream of the mirror. In the lateral extension the far-field boundaries are positioned 3.0 m on opposite sides of the mirror. In the plate-normal direction a far-field boundary is located 3.0 m above the plate. The inlet boundary condition for the DES case follows the "trip-less" approach proposed by Shur et al. [18], with an initial steady state inlet turbulence intensity of 0.1% and a turbulent inlet length scale of 0.1 m followed by a zero inlet turbulent viscosity. For the LES cases no perturbations are applied at the inlet. The cases are summarized in Table 1.

Table 1 requires some additional explanation. The first of the three different grids is (S), a block structured grid generated in ICEM HEXA 5.1 with low Reynolds resolution at the mirror front side. Grid (QS) is a quasistructured grid, where the near-field region is resolved by a block structured hexahedral grid similar to grid type (S) but with finer wake resolution and, to some extent, finer plate resolution. The outer region in the (QS) grid contains a rapidly growing unstructured grid with an overbridging layer of pyramids to enable the node and face. The final grid (U) is a hex-dominant unstructured grid generated in HARPOON 2.4C with isotropic resolution boxes in the mirror wake and above the plate. Closest to the walls, three layers of 1 mm cells resolve the geometry and the near-wall region. Above the plate the maximum cell size permitted is 2 mm, which is kept up to 25 mm perpendicular to the plate. The wake resolution is kept at a maximum of 4 mm at a distance of 0.4 m downstream of the rear side of the mirror. In

Table 1 Description of the conducted cases

	Case parameters			
ID	Grid topology	Turbulence treatment	Spatial discretization scheme	Number of cells ($\times10^6$)
M1SA2UD	S	DES (S-A)	2UD	5.83
M1SABCD	S	DES (S-A)	BCD	5.83
M1DS2UD	S	Dyn Smag	2UD	5.83
M1DSBCD	S	Dyn Smag	BCD	5.83
M1SLBCD	S	Smag–Lilly	BCD	5.83
M2SLBCD	QS	Smag–Lilly	BCD	11.8
M3SLBCD	U	Smag–Lilly	BCD	31.1

this text n^+ will refer to the wall-normal direction, s^+ to the streamwise direction, and l^+ to the lateral direction. At solid boundaries the log-law is applied for cells located in the range of $30<n^+<300$, and the viscous sublayer is assumed to be resolved for cell centroids located at $n^+<5$. A blending of the wall shear stress is carried out in the intermediate region. The log-law is assumed to be valid over a major part of the plate while resolving the viscous sublayer over the front side of the mirror.

The mirror front side n^+ values are less than 1.5 for the (S) and (QS) grids and less than 120 for the (U) grid. Corresponding s^+ and l^+ values are typically 30–40 and 80–90, respectively, for the (S) and (QS) grids and less than 120 in both directions for the (U) grid due to the cubic isotropic cells. Maximum n^+ values occur close to the plate's leading edge and are approximately 400 for grid (S) and 200 for grid (QS). For grid (U) the maximum n^+ is approximately 100 at the plate's leading edge. These levels decrease rapidly downstream of the plate until transition occurs, where they again increases.

For the M2SLBCD case a time-step size of $1\times10e^{-5}$ s was used; for all other cases the time-step size was kept twice as large, i.e., $2\times10e^{-5}$ s. The maximum Courant–Friedrichs–Lewy (CFL) number ranges from $3<\mathrm{CFL}_{\mathrm{conv}}<14$ for the (S) grid depending on the model and $22<\mathrm{CFL}_{\mathrm{conv}}<26$ for the two finer grids (QS) and (U). The maximum levels are typically found close to the trailing edge of the mirror and is limited to just a few cells. All cases cover 0.4 s of physical time.

The different turbulence models are given in column three of Table 1. Starting with DES, one of the most important aspects of the original formulations is to prevent grid-induced separation. No shielding between the inner and outer flows exists in FLUENT, which means that the user has to take an eventual grid-induced separation into account when building the grid. Here, an a priori estimate of the boundary layer thickness is used from a laminar Blasius solution for cylinder flows [9]. At the present Reynolds number the estimated boundary layer thickness is $\delta\approx0.59$ mm, which is resolved by ten cells in the wall-normal direction. To prevent an eventual grid-induced separation in the DES case, the following relation must be fulfilled [19]:

$$C_{\mathrm{DES}}\Delta > \mathcal{O}(1)\delta \tag{1}$$

In Eq. (1), Δ is the maximum extension of the cell, $C_{\mathrm{DES}}=0.65$, and δ is the boundary layer thickness. For cells located at the front side of the mirror close to the trailing edge, this requirement is fulfilled by at least one order of magnitude.

The dynamic Smagorinsky constant C_v is clipped at 0 and 0.23, and the test filter comprises the computational cell and the neighboring cells that share the same faces. For hexahedral cells used in the present work the ratio between the test filter and the grid filter is approximately 2.1 or $9^{1/3}$. The dynamic Smagorinsky constant is solved by seeking C_v for which the error norm E is minimized as follows:

$$E = \left(L_{ij} - \frac{\delta_{ij}}{3}L_{kk} - C_v M_{ij}\right)^2 \tag{2}$$

where

$$M_{ij} = -2(\tilde{\Delta}^2|\tilde{\bar{S}}|\tilde{\bar{S}}_{ij} - \bar{\Delta}^2\widetilde{|\bar{S}|\bar{S}_{ij}}) \tag{3}$$

They then set $\partial E/\partial C_v=0$, resulting in

$$C_v = \frac{L_{ij}M_{ij}}{M_{ij}M_{ij}} \tag{4}$$

For a more detailed description, see Ref. [20].

In the Smagorinsky–Lilly model the eddy viscosity is computed as follows:

$$\nu_t = \rho L_s^2|\bar{S}| \tag{5}$$

where

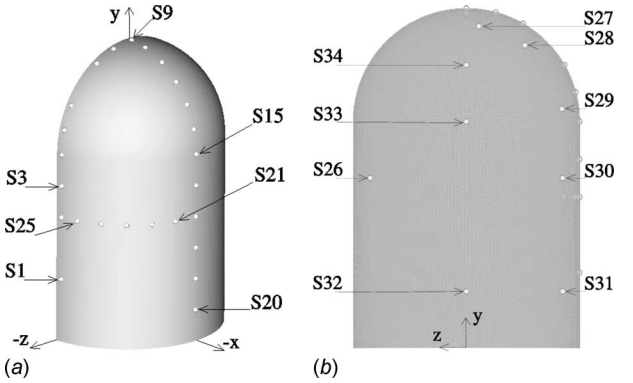

Fig. 3 Location of static pressure sensors over the front and rear side of the mirror: (*a*) Static sensor distribution over the front side and (*b*) static senor distribution over the rear side

$$|\bar{S}| = \sqrt{2\bar{S}_{ij}\bar{S}_{ij}} \tag{6}$$

and

$$L_s = \min(\kappa d, C_s V^{1/3}) \tag{7}$$

In Eq. (7), $C_s=0.1$ and d denotes the distance to the nearest wall.

The advection schemes used for the different cases are presented in column four where (2UD) is a second-order upwind-biased scheme and the (BCD) scheme is the bounded central difference scheme. The BCD scheme is essentially a second-order central scheme with a wiggle detector for wavelengths of $2\Delta x$ or less. For these occasions it locally blends with a second-order upwind scheme or, in the worst case, a first-order upwind scheme.

Figure 3 shows the location of the static pressure sensors. Sensors S1-S25 are located on the front side of the mirror and sensors S26-S34 are located on the rear side of the mirror.

The dynamic pressure sensors are distributed over the plate and the rear side of the mirror according to Fig. 4. The results for the dynamic pressure sensors obtained from Daimler–Chrysler [11] were low pass filtered using a Butterworth filter with a stop-band frequency of 2000 Hz and a bin width of 10 Hz. To reproduce these results the time sequences were resampled and split into windows containing 4096 samples for all cases conducted except for case M2SLBCD, which contained windows sizes of 8192 samples due to a sampling frequency of 100k Hz compared with 50k Hz for the other cases. Furthermore, each window was Hanning filtered with a 50% overlap.

From a wind noise perspective the wall pressure levels are by far the most important result owing to the representation of the physical excitation of the exterior structure. The fluctuating pressure level is computed in the following way:

$$\mathrm{SPL} = 10\log_{10}\frac{\hat{p}}{p_{\mathrm{ref}}^2} \tag{8}$$

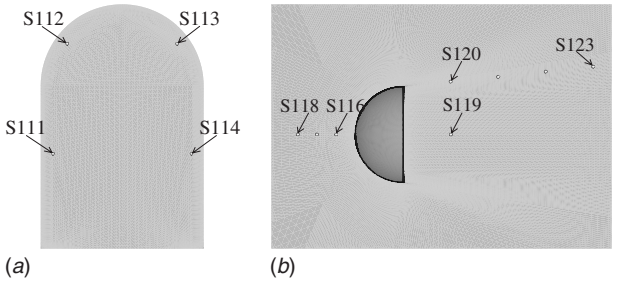

Fig. 4 Location of dynamic pressure sensors over the rear side of the mirror and the plate: (*a*) Dynamic sensor distribution over the rear side and (*b*) dynamic senor distribution over the plate

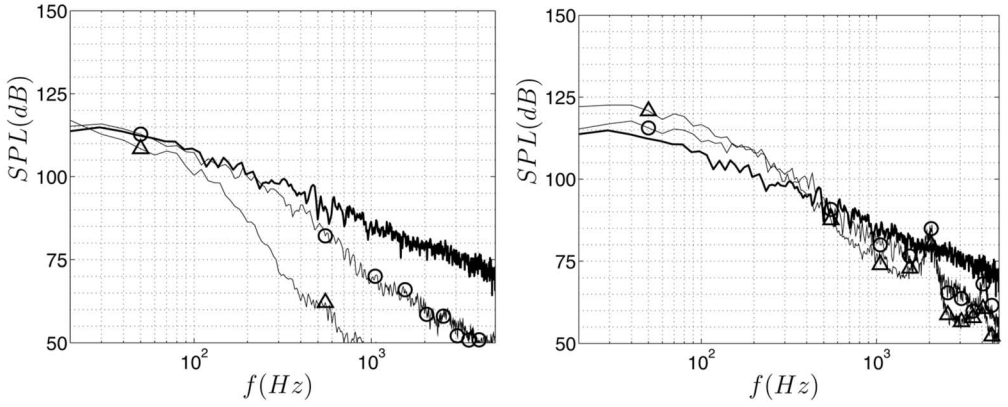

(a) DES model results at sensor S119, Experiment (-), M1SABCD (○), M1SA2UD (△)

(b) Dynamic Smagorinsky model results at S119, Experiment (-), M1DSBCD (○), M1DS2UD (△)

Fig. 5 Effect of advection scheme at sensor S119, DES and Dynamic Smagorinsky models

where $p_{\text{ref}}=2.0\cdot10^{-5}$ Pa is the reference pressure, and $\hat{p}$ is the filtered Fourier transformed results of the fluctuating pressure.

The cutoff frequency is estimated as $f_{\max}=|u_{p,\text{rms}}|/(2\Delta x_p)$, where $u_{p,\text{rms}}$ is the root mean square (rms) of the resolved fluctuating velocity magnitude and Δx_p is the local near-wall grid spacing. The number of grid points per wavelength is estimated as $\lambda_{\max}/\Delta x_p$, where $\lambda_{\max}=U_\infty/f_{\max}$.

4 Effect of Discretization Scheme

The discretization scheme has both a local and a global effect on the flow. The two schemes are thus evaluated as far downstream as possible for two different flow regimes: at the symmetry plane in the mirror wake S119 and at the farthest downstream sensor position S123 in the shear layer of the mirror. The schemes are investigated for both the DES model and for the dynamic Smagorinsky model shown in Figs. 5 and 6.

The LES case results obtained by the two advection schemes return very similar levels at sensor S119 (Fig. 5(*b*)), while the DES model returns significantly lower levels above 100 Hz for the 2UD scheme (Fig. 5(*a*)). Similar trends are also found for sensor S123, with a rapid decay of the fluctuations when the DES model is used in combination with the pure upwind scheme (Fig. 6(*a*)). At sensor S123 the experiments show a peak at approximately 40 Hz, which is best represented by the BCD scheme in combination with the dynamic model. In summary, combining the DES model with the upwind scheme seems to be a truly unsuccessful combination. As early as at 300 Hz the level is at best about 10 dB lower than both the experiments and the BCD scheme. It appears from these results that the BCD scheme is the best choice of the two schemes, primarily due to a low sensitivity to the turbulence model.

5 Effect of Turbulence Treatment

An upstream separation line can clearly be identified in the oil film visualization picture (Fig. 7(*a*)) located at approximately $0.15D$, measured from the rear side edge of the mirror. Instantaneous LES and DES results of the wall shear stress are also presented in Figs. 7(*b*) and 8 and indicate fair agreement in the separation at the front side of the mirror for the LES cases as compared with the experiments (Fig. 7(*a*)). The DES case lacks this feature completely (Fig. 8(*b*)), due to an excessive production of turbulent viscosity preventing the occurrence of the separation.

The downstream effects of the different models are not as apparent (Figs. 9(*a*) and 9(*b*)). At positions S119–S122 the DES model underpredicts the results by about 5 dB at 500 Hz. These effects become less pronounced further downstream and, at posi-

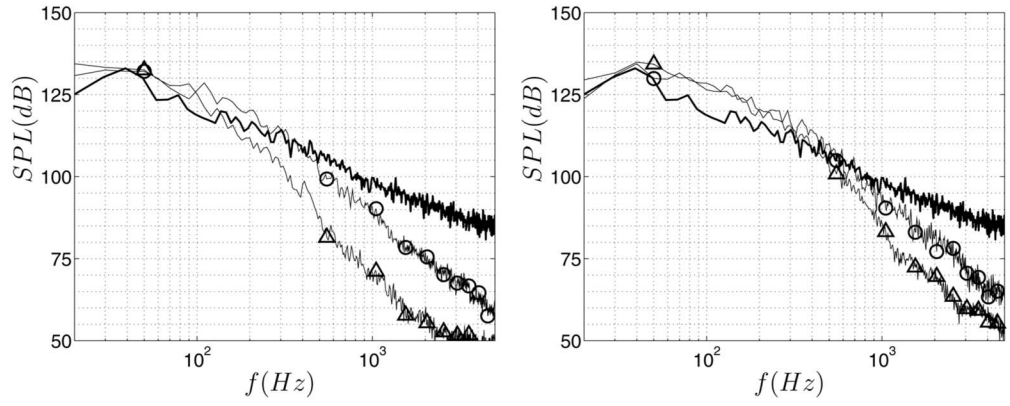

(a) DES model results at sensor S123, Experiment (-), M1SABCD (○), M1SA2UD (△)

(b) Dynamic Smagorinsky model results at S123, Experiment (-), M1DSBCD (○), M1DS2UD (△)

Fig. 6 Effect of advection scheme at sensor S123, DES and Dynamic Smagorinsky model, respectively

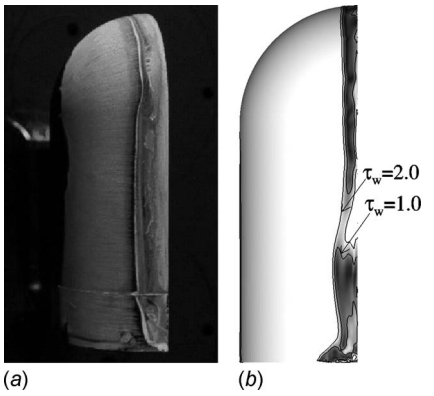

Fig. 7 Oil film visualization and snapshot of wall shear stresses for the M1SLBCD case: (*a*) Oil film visualization (courtesy of Daimler Chrysler Research and Technology), and (*b*) wall shear stress, M1SLBCD, $0<\tau_{wall}<2.0$

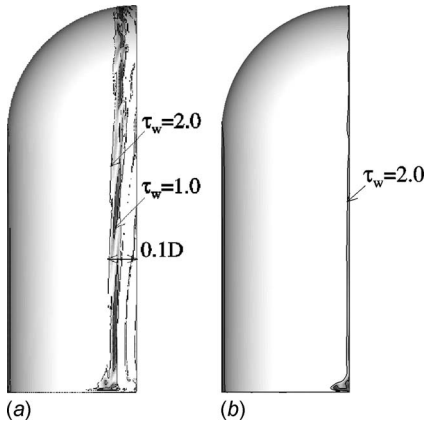

Fig. 8 Snapshot of wall shear stresses for the M1DSBCD and M1SABCD casese: (*a*) Wall shear stress, M1DSBCD, $0<\tau_{wall}<2.0$ and (*b*) wall shear stress, M1SABCD, $0<\tau_{wall}<2.0$

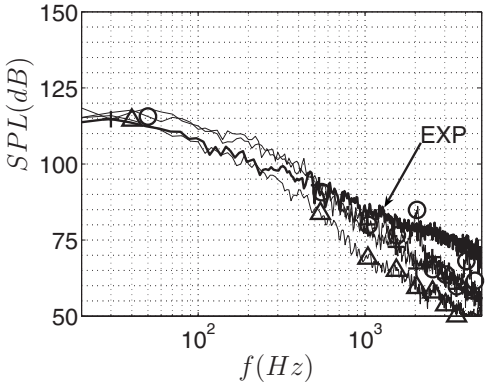

(a) Effect of different turbulence models at sensor S119, Experiments (-), M1DSBCD (○), M1SABCD (△), M1SLBCD (+)

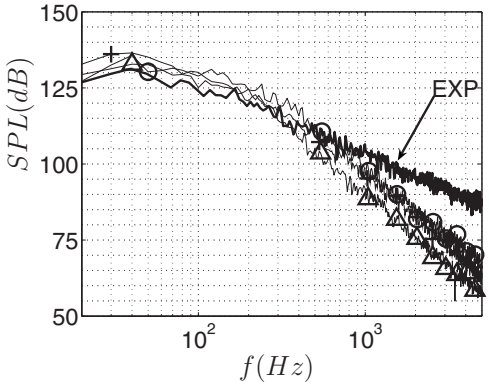

(b) Effect of different turbulence models at sensor S121, Experiments (-), M1DSBCD (○), M1SABCD (△), M1SLBCD (+)

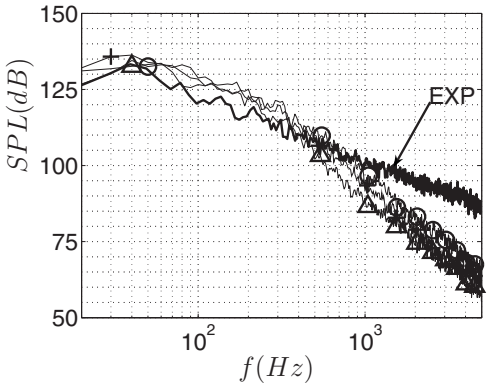

(c) Effect of different turbulence models at sensor S122, Experiments (-), M1DSBCD (○), M1SABCD (△), M1SLBCD (+)

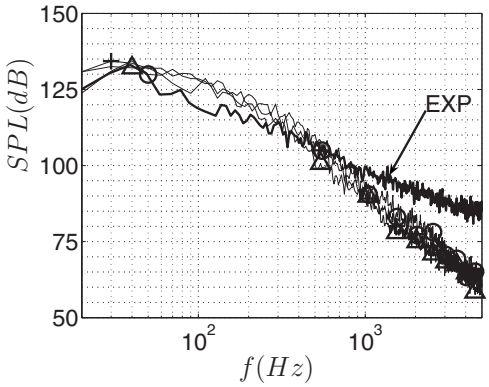

(d) Effect of different turbulence models at sensor S123, Experiments (-), M1DSBCD (○), M1SABCD (△), M1SLBCD (+)

Fig. 9 Effect of different turbulence models

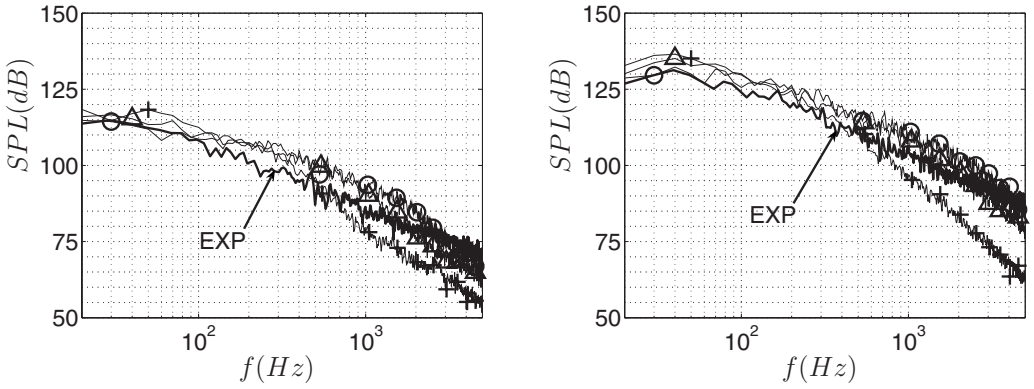

(a) Effect of resolution at sensor S119, Experiment (-), M1SLBCD (+), M2SLBCD (△), M3SLBCD (○)

(b) Effect of resolution at sensor S121, Experiment (-), M1SLBCD (+), M2SLBCD (△), M3SLBCD (○)

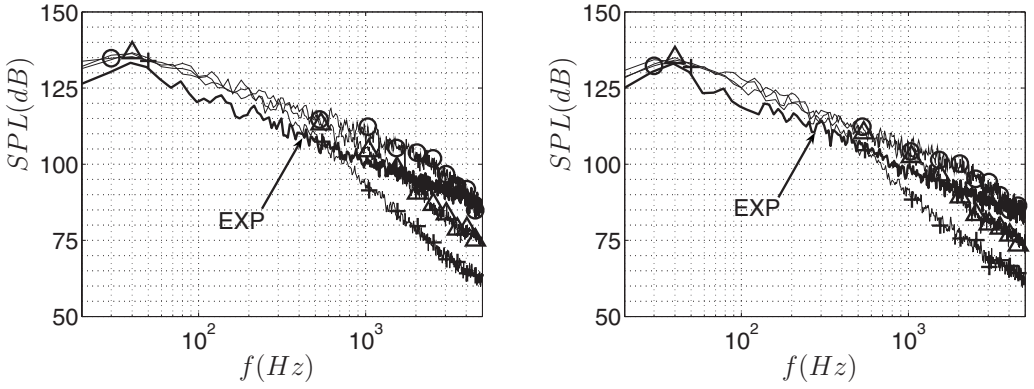

(c) Effect of resolution at sensor S122, Experiment (-), M1SLBCD (+), M2SLBCD (△), M3SLBCD (○)

(d) Effect of resolution at sensor S123, Experiment (-), M1SLBCD (+), M2SLBCD (△), M3SLBCD (○)

Fig. 10 Effect of resolution at four different positions in the mirror wake

tion S123, the differences between the models have almost vanished. Measurements at sensors S121–S123 show a peak at 40 Hz. This peak is fairly well predicted by all models.

A drawback of the dynamic model is the oscillations that occur at multiples of 1000 Hz (Fig. 9(*a*)). Thus, in summary, the DES model seems to underpredict the levels in the near wake of the mirror and the dynamic model shows tendencies to oscillate in the wake. The best candidate among the models investigated is therefore the Smagorinsky–Lilly model, which was also found to be the fastest in terms of CPU hours.

6 Effect of Resolution

The final part of the parameter study primarily contains the effect of different resolution levels. As in Secs 4 and 5 the comparison is made at the four sensor positions in the mirror wake (S119–S123). These results are presented in Figs. 10(*a*)–10(*d*). All simulations return almost identical pressure levels in the frequency range of 20–400 Hz but typically overpredict the level in this region by 5 dB as compared with the experiments. Increased wake and plate resolution has the effect of delaying the decay of the fluctuation levels at increased frequencies (Figs. 10(*a*)–10(*d*)). The trend is however that the 5 dB overprediction found in the low frequency region is present over the whole frequency range. Even though the M3SLBCD case fails to predict the separation point at the front side of the mirror due to the use of wall functions, no apparent effect in the downstream pressure levels can be found.

The computed grid cutoff frequencies at sensors S119–S123 are summarized in Table 2 for the three grids.

The cutoff frequencies in Figs. 10(*a*)–10(*d*) actually mark the starting point for a more pronounced decay of the levels, and a rough estimate is that a 2.5 times finer cell distribution gives a 2.5 times higher grid cutoff frequency.

7 Flow Field Results

In the following text a more thorough examination will be made of the flow field for the case M3SLBCD and, to some extent, case M2SLBCD.

Table 2 Cutoff frequency for the surface sensors

Cutoff frequency for first off-wall cells						
	M1SLBCD		M2SLBCD		M3SLBCD	
Sensor	f_{max} (Hz)	Grid pnts/ λ_{max}	f_{max} (Hz)	Grid pnts/ λ_{max}	f_{max} (Hz)	Grid pnts/ λ_{max}
S119	490	8.3	1210	9.1	1950	10
S121	671	4.8	1670	5.4	3900	5
S122	709	4.5	1590	5.6	3975	4.9
S123	582	5.5	1460	6.1	3475	5.6

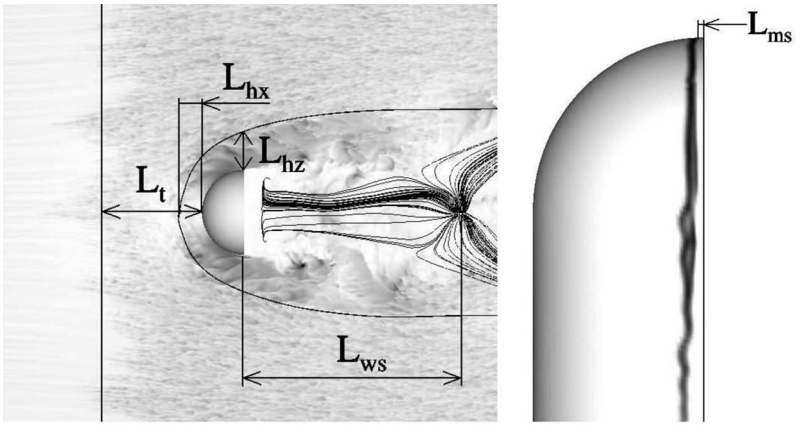

(a) Plate flow structures, M3SLBCD (b) Mirror flow structures, M2SLBCD

Fig. 11 Characterization of dominating flow structures

Freestream air reaches the plate's leading edge forming a laminar boundary layer at the farthest upstream part of the plate (Fig. 11). Local transition streaks occur further downstream of the plate (at L_t upstream of the mirror) and, at approximately $0.5D$ upstream of the mirror, the plate's boundary layer is fully turbulent. Along the symmetry plane of the mirror the flow becomes stagnant as it approaches the front side of the mirror, which results in a horseshoe vortex centered approximately 6 mm above the plate and at position L_{hx} in the streamwise direction (Table 3). At the trailing edge of the mirror close to the plate, shedded vortices interact with the plate's boundary layer causing two symmetric regions with high pressure fluctuations. Their directions with respect to the symmetry plane of the mirror are mainly determined by the mirror wake and, to some extent, the size and proximity of the horseshoe vortex L_{hz}. Above the plate boundary layer undisturbed freestream air meets the front side of the mirror and accelerates along its surface. The boundary layer of the mirror remains laminar until separation occurs close to the mirror's trailing edge. The center of this recirculation bubble is located at the distance L_{ms} from the mirror's trailing edge. Judging from Fig. 11(*b*) versus Fig. 7(*a*) the simulations show a delayed separation point as compared with the experiment. This laminar separation is the starting point for the mirror's wake and the recirculation zone that ends at L_{ws}.

The location of the static pressure sensors were shown in Fig. 3 and the results for these locations are presented in Fig. 12 for both the M2SLBCD and M3SLBCD cases as well as the experimental results [11]. Sensors S1–S9 in region (I) are located 6 mm upstream of the mirror's rear side (Fig. 3(*a*)). Judging from the oil film visualization (Fig. 7(*a*)), their locations are in the flow separated region. All simulations conducted indicate a delayed separation point or fail to predict this feature completely compared with the experiments, which results in an excessive velocity magnitude and a lower pressure as a consequence (Fig. 12). Sensors in region (II) are located along the mirror's symmetry plane starting with the most topward positioned point S10 located 2.6 mm upstream of the mirror's trailing edge. The flow is attached at this sensor position while the measured flow has detached causing a higher pressure as compared with the simulations. At sensors S11 to S20, experimental and simulated mean pressures match perfectly and converge toward $C_p = 1.0$ at the last sensors in this region. Sensor region (III) is located at the mirror's front side 133 mm above the plate. As for sensor S10, sensor S25 is positioned at 2.6 mm, measured from the mirror's trailing edge, and again highlights the misrepresentation of the separation point in the simulations. Both simulations show an even lower pressure at S25 as compared with that at sensor S10 and thus indicate a higher flow speed at this location as compared with sensor S10. The mean pressure over the front side of the mirror shows otherwise good agreement with the experimental results and, on the rear side, region (IV), almost perfect agreement between the two LES cases and the experiment is obtained, even though the M3SLBCD case uses wall functions over the whole front side of the mirror.

Figure 13(*a*) shows the spectral content of lateral and streamwise force coefficients. In the lateral force coefficient a peak is found at 18.3 Hz. A much weaker peak is also found for the streamwise force coefficient at a frequency of 36.5 Hz. The lateral force coefficient is believed to relate to the vortex shedding by a

Table 3 Locations of flow structures found

Identification	Mirror offset (m)
L_t	0.208
L_{hx}	0.0525
L_{hz}	0.0906
L_{ws}	0.5165
L_{ms}	0.002

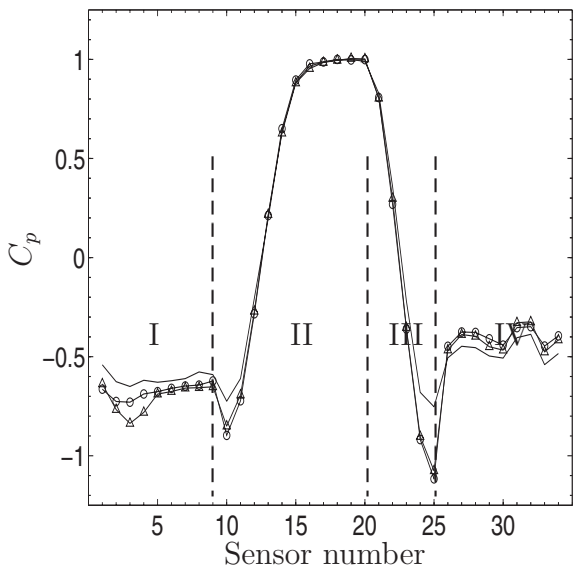

Fig. 12 Mean pressure over mirror: (-) measured, (△) M2SLBCD, and (○) M3SLBCD

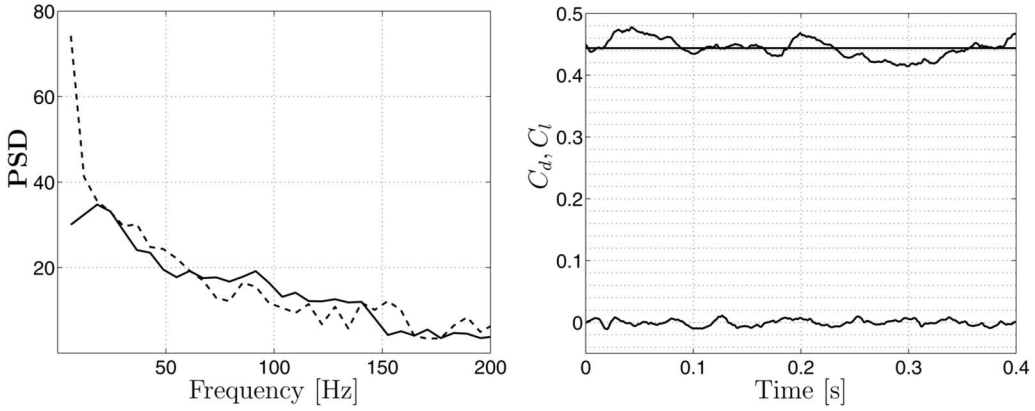

(a) Power Spectral Density versus frequency,(−) lateral force coefficient, (−−) streamwise force coefficient

(b) Time traces of streamwise and lateral mirror forces

Fig. 13 Force coefficient results for the M3SLBCD case

factor of two since two vortices, one rotating clockwise and one co-rotating vortex, are contained within one full period. This shedding frequency, 36.5 Hz, corresponds to the peak found in the mirror's shear layer at sensors S121 to S123 and results in a Strouhal number based on the mirror diameter and the freestream velocity of approximately S_t=0.19. This means that 14 vortex sheddings are contained in the present simulations. Figure 13(*b*) gives the time traces for both the streamwise and lateral force coefficients together with the time-averaged streamwise force coefficient, which is computed to be $\overline{C_d}$=0.4437.

8 Surface Pressure Fluctuations Results

Contours of the mirror and plate pressure fluctuations are shown in Fig. 14 together with the locations of the dynamic pressure sensors. The highest levels are recovered at the plate close to sensors S120 to S123 at the breakup of the detached mirror shear layer. The levels in this region are more than twice as large as over the rear side of the mirror. Upstream of the mirror the horseshoe vortex leaves a clear footprint on the plate, indicating fluctuation levels exceeding the maximum levels at the mirror's rear side.

Pressure fluctuations returned by the dynamic pressure sensors as well as the corresponding computed signals for the M3SLBCD case are presented in the frequency plane in Figs. 15–20. The locations of these sensors are given in the Appendix and, visually, in Fig. 14.

Four sensors are located at the mirror rear side, S111–S114, and the results for these sensors are shown in Figs. 15(*a*) and 15(*b*) The fluctuations at the rear side of the mirror are determined mainly by flow structures in the wake and are accurately predicted up to the grid cutoff frequency indicated by the vertical line. The four sensors show no tonal content and the fluctuations decay rapidly with increased frequency up to the predicted cut-off frequencies.

Sensors S116–S118 are located upstream of the mirror along the mirror's symmetry plane. It is obvious that their purpose is to capture the horseshoe vortex in front of the mirror. S116 is the sensor located closest to the mirror and the levels at this position are accurately predicted up to 1500 Hz with a peak level of about 120 dB, which is significantly higher than the levels at the mirror's rear side. The result for sensor S117 is similar to that for sensor S116, indicating that both sensors are located close to the horseshoe vortex core. Compared with the mirror's rear side sensors, both sensors show a flat low frequency part between 20 Hz and 200 Hz where most of the energy is concentrated. Above this region the levels decay rapidly, contrary to the result for sensor S118. The sensor located farthest upstream S118, shows significantly lower levels as compared with sensors S117 and S116, and the simulation overpredicts the levels by approximately 10 dB. A possible explanation is too early a transition point along the plate, but no experimental results exist to justify this hypothesis. Among the sensors investigated this sensor also turns out to have the flattest curve and indicates a signal with a white noise character and no dominating frequencies. Similar to sensors S116, S117, and S118, sensor S119 is located along the mirror's symmetry plane but is, in contrast, located in the wake downstream of the mirror. The trend for this sensor is similar to that of the sensors at the rear side of the mirror but has a slower decay of the fluctua-

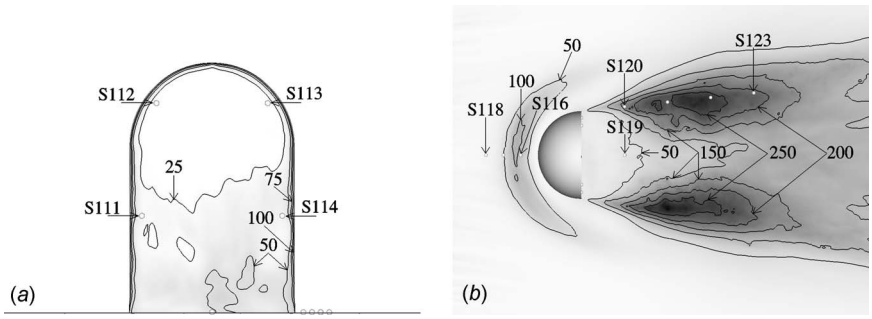

Fig. 14 RMS of wall pressure (Pa) and sensor positions for the M3SLBCD case: (*a*) RMS of pressure on the rear side of the mirror and (*b*) RMS of pressure fluctuations over the plate

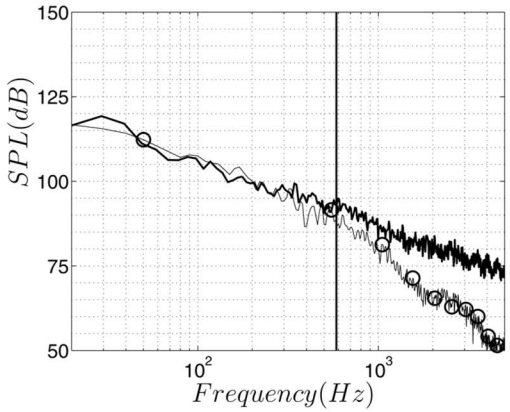

(a) SPL at surface sensor S111, (-) Measured, (○) M3SLBCD

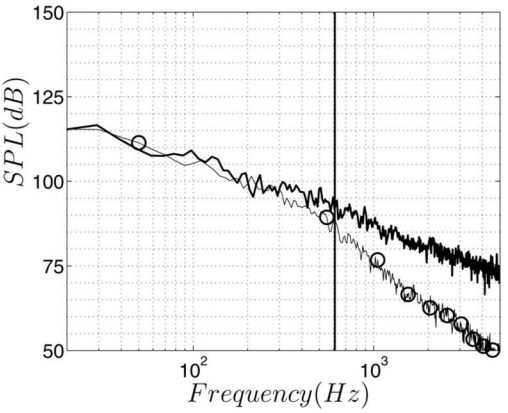

(b) SPL at surface sensor S114, (-) Measured, (○) M3SLBCD

Fig. 15 SPL at sensors S111 and S114

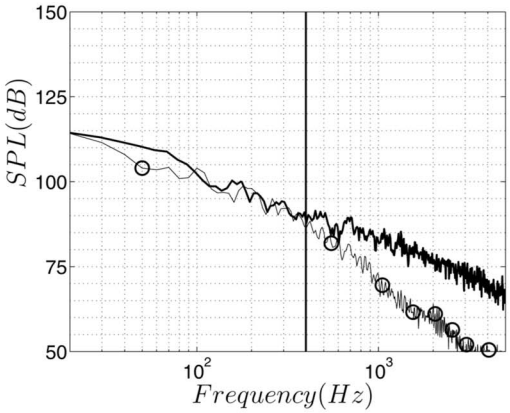

(a) SPL at surface sensor S112, (-) Measured, (○) M3SLBCD

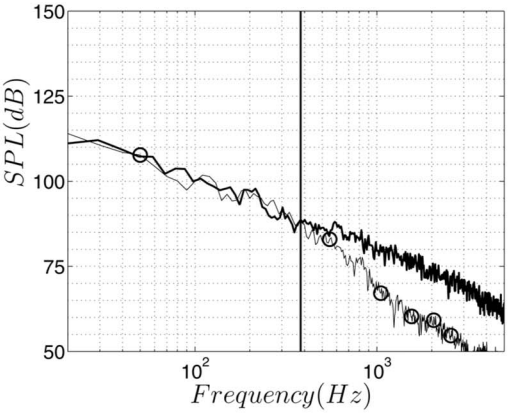

(b) SPL at surface sensor S113, (-) Measured, (○) M3SLBCD

Fig. 16 SPL at sensors S112 and S113

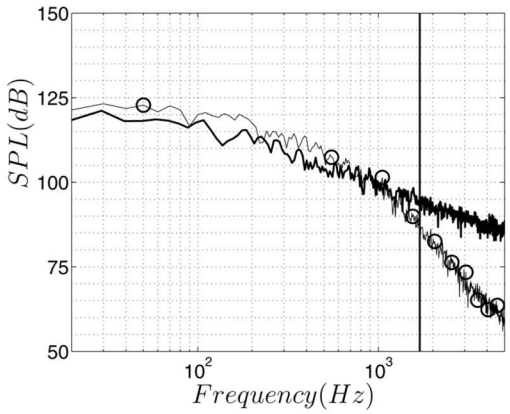

(a) SPL at surface sensor S116, (-) Measured, (○) M3SLBCD

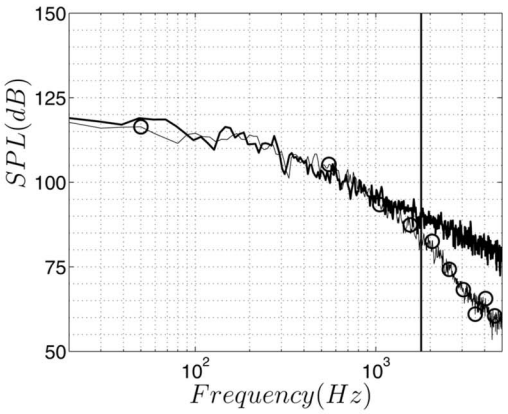

(b) SPL at surface sensor S117, (-) Measured, (○) M3SLBCD

Fig. 17 SPL at sensors S116 and S117

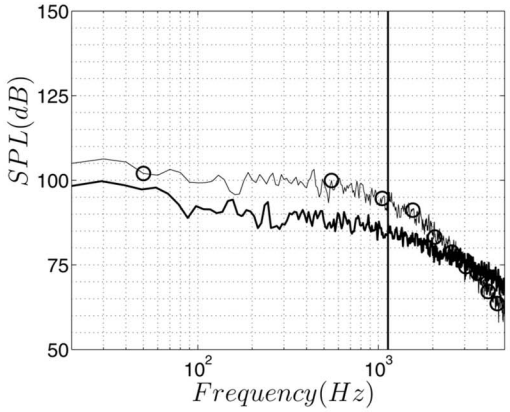

(a) SPL at surface sensor S118, (-) Measured, (∘) M3SLBCD

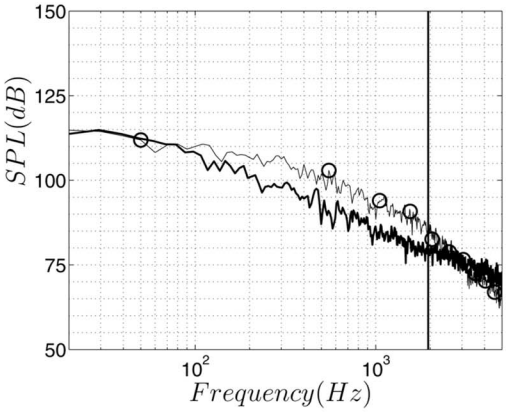

(b) SPL at surface sensor S119, (-) Measured, (∘) M3SLBCD

Fig. 18 SPL at sensors S118 and S119

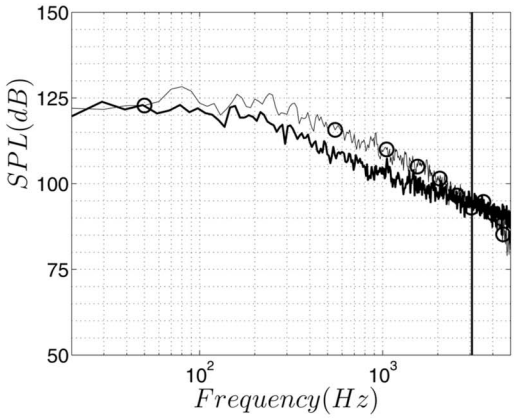

(a) SPL at surface sensor S120, (-) Measured, (∘) M3SLBCD

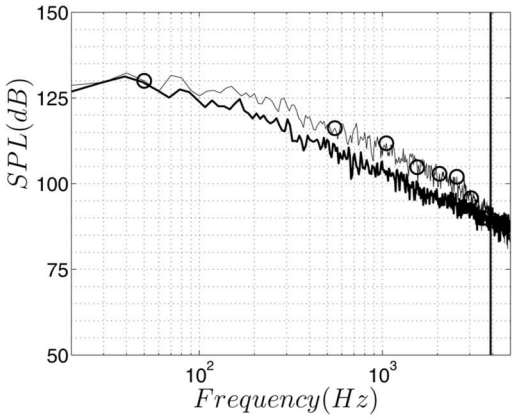

(b) SPL at surface sensor S121, (-) Measured, (∘) M3SLBCD

Fig. 19 SPL at sensors S120 and S121

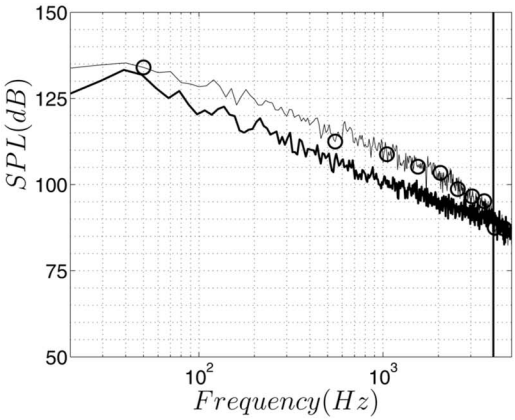

(a) SPL at surface sensor S122, (-) Measured, (∘) M3SLBCD

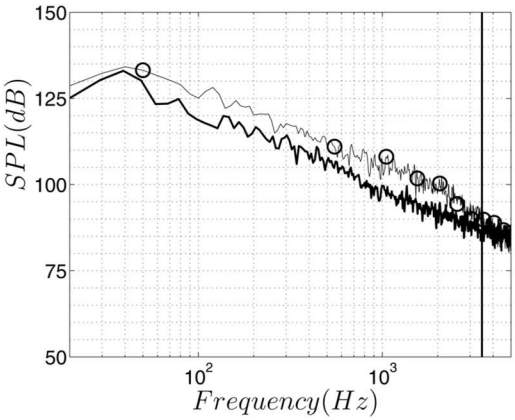

(b) SPL at surface sensor S123, (-) Measured, (∘) M3SLBCD

Fig. 20 SPL at sensors S122 and S123

tions as compared with these sensors, which is explained by its more downstream position, where there exists a wider range of scales.

Sensors S120 and S121 are those positioned farthest upstream in the mirror's shear layer; the results are shown in Figs. 19(*a*) and 19(*b*). The results in the case of sensor S120 are similar to those for sensor S116, with a flat low frequency region followed by a rapid decay at increasing frequencies. At sensor S121, 0.1 m downstream of sensor S120, the signal character changes slightly to gain a more tonal character with a peak at approximately 40 Hz. This peak becomes more pronounced further downstream at sensors S122 and S123 (Figs. 20(*a*) and 20(*b*)).

A general trend in the wall pressure results is that the levels are perfectly predicted at the rear side of the mirror and at the plate upstream of the front side of the mirror. In the mirror's wake and along the mirror's shear layer the simulation catches the trends perfectly but overpredicts the fluctuations by about 5 dB.

9 Conclusion

This paper covers predictions of both the flow field and the acoustic sources of a generic side mirror mounted on a flat plate. The Reynolds number is 5.2×10^5 based on the diameter of the mirror and the corresponding Mach number for this flow field is $Ma_\infty=0.11$. Owing to the low Mach number, the flow field is solved on the basis of an assumption of incompressibility. In the first part of the paper a parameter study is conducted by means of different advection schemes, turbulence models, and three levels of grid resolution. The general outcome of the work is as follows.

An estimation of the local grid cutoff is given by relating the velocity fluctuation with the near-wall grid spacing. This estimate first of all marks the starting point for a more rapid decay of the fluctuation levels. Second, for most sensors, it also marks the frequency at which the simulated results cross or leave the measured levels. This technique is shown to predict the grid cutoff for both structured and unstructured grids.

The choice of advection scheme, i.e., a second-order upwind or second-order hybrid scheme, has little effect on the downstream pressure fluctuations as long as the DES model is avoided.

As concerns turbulence modeling, the DES model should be avoided if fluctuations are of interest. Both the dynamic model and the Smagorinsky–Lilly model with near wall damping give a significant improvement in the representation of the wide range of turbulent scales and have the potential to capture both the laminar separation point and the point of transition from a laminar to a turbulent boundary layer. Although the dynamic model and the Smagorinsky–Lilly model give similar results, oscillations are to be expected when using the dynamic model, which suggests that the simpler Smagorinsky–Lilly model is preferable.

The computed mean pressure levels at the mirror surface are in good agreement with the experimental results except for the sensors located near the mirror laminar separation line and are fairly independent of whether the mirror's boundary layer is resolved or replaced by wall functions. The computed shedding frequency is 37 Hz based on the lateral force coefficient, resulting in a Strouhal number of about $S_t=0.19$, and the mean streamwise force coefficient is computed to be $\overline{C_d}=0.4437$ on the basis of the projected area of the mirror.

The fundamental frequency based on the spectral peaks at sensors S121–S123 were both computed and found from the experiments to be approximately $f_n=40$ Hz. The fundamental frequency based on convection of the shear layer disturbances is due to the alternating rotating vortices from the shear layer instabilities, with twice as high a frequency as the lateral force coefficient, which supports the findings regarding the Strouhal number. A perfect match between measured and computed results is found for sensors located at the rear side of the mirror and upstream of the mirror at the mirror's symmetry plane. One exception exists however for sensor S118, indicating a possibly too early a transition point in the simulation. All sensors in the mirror's wake and in the mirror's shear layer captures the trends perfectly but show an overprediction of the intermediate frequency region by about 5 dB in the case of the simulations.

Acknowledgment

This work was supported by the Volvo Car Corporation and the Swedish Agency for Innovation Systems (VINNOVA). We would also like to express our gratitude to Dr. Franz R. Klimetzek at Daimler Chrysler, who let us use their experimental data and pictures.

Appendix

Table 4 shows the locations of the static and dynamic sensors.

Table 4 Location of dynamic and static pressure sensors

Positions of dynamic pressure sensors			
Sensor ID	*x*	*y*	*z*
S111	0.100	0.1167	0.0850
S112	0.100	0.2517	0.0674
S113	0.100	0.2517	−0.0674
S114	0.100	0.1167	−0.0850
S116	−0.0400	0.00	−0.0000
S117	−0.0800	0.00	−0.0000
S118	−0.1200	0.00	−0.0000
S119	0.2000	0.00	−0.0000
S120	0.1995	0.00	−0.1105
S121	0.2989	0.00	−0.1209
S122	0.3984	0.00	−0.1314
S123	0.4978	0.00	−0.1418
Positions of static pressure sensors			
Sensor ID	*x*	*y*	*z*
S1	0.0940	0.0667	−0.0998
S2	0.0940	0.1333	−0.0998
S3	0.0940	0.1667	−0.0998
S4	0.0940	0.2000	−0.0998
S5	0.0940	0.2258	−0.0964
S6	0.0940	0.2499	−0.0864
S7	0.0940	0.2864	−0.0499
S8	0.0940	0.2964	−0.0258
S9	0.0940	0.2998	0.0000
S10	0.0741	0.2966	0.0000
S11	0.0500	0.2866	0.0000
S12	0.0293	0.2707	0.0000
S13	0.0134	0.2500	0.0000
S14	0.0034	0.2259	0.0000
S15	0.0000	0.2000	0.0000
S16	0.0000	0.1667	0.0000
S17	0.0000	0.1333	0.0000
S18	0.0000	0.1000	0.0000
S19	0.0000	0.0667	0.0000
S20	0.0000	0.0333	0.0000
S21	0.0034	0.1333	−0.0259
S22	0.0134	0.1333	−0.0500
S23	0.0293	0.1333	−0.0707
S24	0.0500	0.1333	−0.0866
S25	0.0741	0.1333	−0.0966
S26	0.1000	0.1500	0.0850
S27	0.1000	0.2843	−0.0111
S28	0.1000	0.2674	−0.0517
S29	0.1000	0.2111	−0.0843
S30	0.1000	0.1500	−0.0850
S31	0.1000	0.0500	−0.0850
S32	0.1000	0.0500	0.0000
S33	0.1000	0.2000	0.0000
S34	0.1000	0.2500	0.0000

References

[1] Höld, R., Brenneis, A., and Eberle, A., 1999, "Numerical Simulation of Aeroacoustic Sound Generated by Generic Bodies Placed on a Plate: Part I—Prediction of Aeroacoustic Sources," Fifth AIAA/CEAS Aeroacoustics Conference, Seattle, WA, May 10–12, Paper No. AIAA-99-1896.

[2] Siegert, R., Schwartz, V., and Reichenberger, J., 1999, "Numerical Simulation of Aeroacoustic Sound Generated by Generic Bodies Placed on a Plate: Part II—Prediction of Radiated Sound Pressure," Fifth AIAA/CEAS Aeroacoustics Conference, Seattle, WA, May 10–12, Paper No. AIAA-99-1895.

[3] Rung, T., Eschricht, D., Yan, J., and Thiele, F., 2002, "Sound Radiation of the Vortex Flow Past a Generic Side Mirror," Eighth AIAA/CEAS Aeroacoustics Conference, Breckenridge, CO, Jun. 17–19, Paper No. AIAA-2002-2340.

[4] EXA, 2003, "Validation Update: Model Mirror," Aeroacoustic Consortium 2003/2004 Presentation, Aug. 20.

[5] Bipin, L., Sandeep, S., and Jieyong, X., 2003, "Computational Aeroacoustic Analysis of a Generic Side View Mirror," Noise and Vibration Conference and Exhibition, Traverse City, MI, May 5–8, Paper No. SAE-2003-01-1698.

[6] Ffowcs Williams, J. E. and Hawkings, D. L., 1969, "Sound Generation by Turbulence and Surfaces in Arbitrary Motion," Philos. Trans. R. Soc. London, Ser. A, **264**(1151), pp. 321–342.

[7] Brentner, K. S. and Farassat, F., 2003, "Modeling Aerodynamically Generated Sound of Helicopter Rotors," Prog. Aerosp. Sci., **39**, pp. 83–120.

[8] Spalart, P., Jou, W.-H., Strelets, M., and Allmaras, S. R., 1997, "Comments on the Feasibility of LES for Wings, and on a Hybrid RANS/LES Approach," First AFOSR International Conference on DNS/LES. Advances in DNS/LES, pp. 137–147.

[9] Schlichting, H., 1969, *Boundary Layer Theory*, Springer, New York.

[10] Constantinescu, G. S. and Squires, K. D., 2003, "LES and DES Investigations of Turbulent Flow Over a Sphere at Re=10000," Flow, Turbul. Combust., **70**, pp. 267–298.

[11] Klimetzek, F., 2005, private communication.

[12] Strelets, M., 2001, "Detached Eddy Simulation of Massively Separated Flows," 39th AIAA Aerospace Sciences Meeting and Exhibit, Reno, NV, Jan. 8–11, Paper No. AIAA-2001-0879.

[13] Constantinescu, G. S. and Squires, K. D., 2004, "Numerical Investigations of Flow Over a Sphere in the Subcritical and Supercritical Regimes," Phys. Fluids, **16**, pp. 1449–1466.

[14] Spalart, P., Hedges, L., Shur, M., and Travin, A., 2003, "Simulation of Active Flow Control on a Stalled Airfoil," Flow, Turbul. Combust., **71**, pp. 361–373.

[15] Hedges, L. S., Travin, A. K. and Spalart, P., 2002, "Detached-Eddy Simulations Over a Simplified Landing Gear," ASME J. Fluids Eng., **124**, pp. 413–423.

[16] Schmidt, S. and Thiele, F., 2003, "Detached Eddy Simulation of Flow Around A-Airfoil," Flow, Turbul. Combust., **71**, pp. 261–278.

[17] FLUENT Inc., 2004, FLUENT 6.2 Documentation.

[18] Shur, M., Spalart, P., Strelets, M., and Travin, A., 1996, "Navier–Stokes Simulation of Shedding Turbulent Flow Past a Circular Cylinder and a Cylinder With Backward Splitter Plate," Computational Fluid Dynamics '96, Proceedings of the Third ECCOMAS Computational Fluid Dynamics Conference, Sept. 9–13, pp. 676–682.

[19] Menter, F., Kuntz, M., and Bender, R., 2003, "A Scale-adaptive Simulation Model for Turbulent Flow Predictions," 41st Aerospace Science Meeting and Exhibit, Jan. 6–9, Paper No. AIAA-2003-0767.

[20] Kim, S. E., 2004, "Large Eddy Simulation Using Unstructured Meshes and Dynamic Subgrid-Scale Turbulence Model," 34st AIAA Fluid Dynamics Conference and Exhibit, Jun., Paper No. AIAA-2004-2548.